EUROPEAN FUSION DEVELOPMENT AGREEMENT

EFDA–JET–PR(03)51

T. Onjun, G. Bateman, A. Dnestrovskij, G. Huysmans, A.H. Kritz, J. Lönnroth,
V. Parail, H. Wilson and JET EFDA contributors

Stability Analysis of H-mode Pedestal and ELMs in a JET Power Scan

Stability Analysis of H-mode Pedestal and ELMs in a JET Power Scan

T. Onjun[1], G. Bateman[1], A. Dnestrovskij[2], G. Huysmans[3], A.H. Kritz[1], J. Lönnroth[4], V. Parail[5], H. Wilson[5] and JET EFDA contributors*

[1]Lehigh University Physics Department, 16 Memorial Drive East, Bethlehem, PA 18015
[2]Russian Science Centre Kurchatov Institute, Moscow, Russia
[3]Association EURATOM-CEA, CEA Cadarache, DRFC, Batiment 513, 13108 Saint-Paul-Lez-Durance, France
[4]Association EURATOM-Tekes, Helsinki University of Technology, P.O. Box 2200, 02015 HUT, Finland
[5]EURATOM/UKAEA Fusion Association, Culham Science Centre, Abingdon Oxon OX14 3DB, UK
** See annex of J. Pamela et al, "Overview of Recent JET Results and Future Perspectives", Fusion Energy 2000 (Proc. 18th Int. Conf. Sorrento, 2000), IAEA, Vienna (2001).*

Preprint of Paper to be submitted for publication in
Physics of Plasmas

ABSTRACT.
Simulations of three JET H-mode discharges in a power scan are carried out using the JETTO integrated modeling code with predictive core and pedestal models, which include the effect of ELMs. It is found that current-driven peeling modes trigger the ELM crashes in these discharges and, as a result, yield an explanation of the increase in pedestal height with heating power. After each ELM crash, the bootstrap current density and the related pressure gradient rapidly increase with increasing heating power, while the total current density rises only slowly because the total current density is impeded by a back EMF. Hence, as the heating power is increased, the pedestal pressure can rise to higher values during an ELM cycle before the current density reaches the level required for destabilization of the current-driven peeling modes. A stability analysis using the MISHKA code is carried out in conjunction with these simulations. The analysis includes infinite-*n* ideal ballooning, finite-*n* ballooning and low-*n* kink (peeling) modes.

1. INTRODUCTION

Energy connement in the high-confinement (H-mode) regime of tokamaks is found to be quite sensitive to the nature of the pedestal that forms at the edge of H-mode plasmas. The pedestal is a narrow region located near the separatrix, typically occupying less than 5% of the plasma minor radius. It was found in a JETpower scan that the pedestal height increases with increasing heating power [1]. It is important to understand the physical processes that produce this dependence of pedestal height on heating power in order to develop an improved pedestal model. An improved model is needed for the prediction of plasma profiles in future experiments and of the performance of burning plasma experiments such as ITER [2].

It is found that the pedestal height is independent of heating power when based on the pedestal model in which the pressure gradient near the edge of plasma is limited by the critical pressure gradient of the ballooning mode without the eect of time-dependent Edge Localized Modes (ELMs) [3, 4]. On the other hand, a pedestal model based on concept of thermal conduction [4] yields the pedestal height that increases with heating power. A comparison between the pedestal model using the MHD ballooning approach and a pedestal model based on the thermal conduction approach was carried out in Ref. [4]. When compared with experimental data, the thermal conduction pedestal model (Eq. (2) in Ref. [4]) yielded an RMSE of 23.5% while the ballooning mode pedestal model (Eq. (5) in Ref. [4]) yielded an RMSE of 25.0%. Consequently, in that study, the level of agreement of both pedestal models with experimental data was comparable.

In this paper, the role of heating power in the prediction of the pedestal height is investigated by examining three JET discharges in a power scan. The discharges are type I ELMy H-mode with similar plasma parameters, except for the heating power. It was found that the measured pedestal stored energy and the measured temperatures at the top of the pedestal in these JET discharges increase as the heating power increases [1]. An integrated predictive modeling code, JETTO [5], is used to carry out simulations of the core and edge plasma for these three JET discharges in order to

understand the physical processes that produce this experimental trend. MHD equilibrium and stability analyses codes, HELENA and MISHKA [6], are used to evaluate the edge stability in these simulations. The instabilities considered include the infinite-*n* ideal ballooning, finite-*n* ballooning, and low-*n* kink (peeling) modes. The results from these simulations and their stability analyses yield a better understanding of the role of heating power in the pedestal physics.

This paper is organized as follows. The transport code, JETTO, and equilibrium and stability codes, HELENA and MISHKA, are described in Section II. In Section III, the details of the three discharges considered in this paper are described with some discussions regarding an experimental observation. Simulation results and a stability analysis of these simulations are presented in Section IV, followed by conclusions in Section V

2. MODELLING CODES

In this paper, simulations of the JET power scan are carried out using predictive JETTO code, while the MHD stability analysis involves use of the HELENA and MISHKA codes. These codes are described in this section.

2.1. THE JETTO CODE

The $1^1/_2$ D JETTO transport code is used to evolve the plasma current, temperatures and density profiles in both the core and pedestal regions. The core transport is calculated using the Mixed Bohm/gyro-Bohm model [7]. For the pedestal region, two assumptions are used in this paper. One assumption is that the turbulent transport is completely suppressed in the region between the top of the pedestal and the separatrix. For simplicity, all the diagonal elements of the transport matrix within the pedestal are taken to be the ion neoclassical thermal conductivity, calculated at the top of the pedestal. The pedestal width is usually of the order of the ion orbit width (or banana width), which implies limited variation of the neoclassical transport across the barrier. The second assumption regarding the pedestal is that of the pedestal width is either axed width of 3cm, or a width proportional to the ion Larmor radius. It will be shown later that the variation of the pedestal width by itself is not sufficient to explain the experimental trend observed in this JET power scan.

An anomalous transport is assumed to be presented in the core but suppressed within the pedestal region. The reduced transport within the pedestal results in the development of a steep pressure gradient within the pedestal region. This sharp pressure gradient causes an increase in the bootstrap current within the edge transport barrier. The increase of the edge pressure gradient and the resulting increase in edge current density eventually leads to a destabilization of MHD modes. This destabilization then triggers an ELM crash, which results in a loss of plasma energy and particles to the wall. The destabilization is considered to be due to either a pressure-driven ballooning mode [8, 9] or a current-driven peeling mode [10, 11, 12, 13].

In exercising the JETTO code, one of two options is employed. In one option, the pressure gradient is allowed to increase until the pressure gradient anywhere within the edge transport barrier

exceeds the critical pressure gradient of the ballooning mode. The second option is to allow the pedestal pressure and current to increase until the current-driven peeling mode criterion is satised. With either option, when the instability criterion is met, an ELM crash occurs. Note that the criterion used for the current-driven peeling mode instability is that the edge current density exceeds the critical value predicted using an analytical expression developed in Ref. [11]. When the condition for an ELM crash is satised, all diagonal transport coefficients in the JETTO code are temporarily increased by 300 times ion neoclassical at the top of the pedestal for electron and ion thermal transport and 100 times ion neoclassical at the top of the pedestal for particle transport within the pedestal for the specied time interval $\tau_{ELM} = 0.4$ms, which is of the order of a typical ELM duration in JET type I ELMy H-mode discharges. The large increase of the transport within the pedestal leads to a loss of particles and energy, similar to the loss during an ELM crash in the experiment.

2.2 MHD STABILITY CODES

In this paper, an MHD stability analysis has been carried out using the HELENA and MISHKA codes [6]. HELENA is used to refine the equilibrium and to compute the stability of infinite-*n* ideal ballooning modes. The HELENA code takes plasma profiles and equilibrium information, generated by JETTO, to produce an equilibrium with the higher resolution that is needed for the MISHKA code. MISHKA is then used to evaluate the stability criteria for finite-*n* ballooning and low-*n* kink (peeling) modes. In this study, the stability analysis carried out with the MISKHA code is for modes with toroidal mode number $n = 1$to $n = 14$. Note that the version of the MISHKA code used in this paper is based on the ideal MHD model.

3. EXPERIMENTAL BACKGROUND

Three JET type I ELMy H-mode discharges in a power scan [1], JET discharge 44018, 44029 and 44013, are considered in this study. These discharges have the same plasma current, magneticeld, elongation and triangularity, but dierent heating power. Some of the plasma parameters for these discharges are given in Table I. Figure 1 shows the time history of the D_α signal measured at the edge of the plasma, as well as the stored energy and the heating power for the three discharges. For each discharge, it can be seen that the stored energy is roughly constant during the quasi-steady state H-mode period from 18.0s to 20.0s, and that the stored energy is greater in the discharges with increased heating power.

In Ref. [14], the scaling of the heating power required the transition from L-mode to H-mode, P_{LH}, is expressed as

$$P_{L-H}\,(\mathrm{MW}) = 2.84 A_H^{-1}\, B_T^{0.82}\, \bar{n}_{20}^{-0.58}\; R^{1.00}\, a^{0.81} \qquad (1)$$

where $\bar{n}_{20}$ is the line average density in units of 10^{20} particles/m^3. Note, the notation and units used in this paper are described in Table II. Based on Eq. 1, the L-H transition power ranges between 6.4

and 6.6 MW for the three discharges considered. These three JET discharges, 44018, 44029 and 44013, are heated mainly by the NBI heating with the power ranging from 8.1MW to 13.9MW, which is signicantly higher than the power required for the transition to H-mode.

The temperature, density and pressure at the top of the pedestal before an ELM crash is given in Table III. Note that the values in Table III are obtained from the ITPA Pedestal Database [15] version 3.1. In this database, the pedestal density and temperatures are found by using a lineart to each pedestal prole. It can be seen from Table III that the electron pressure and electron temperature at the top of the pedestal increase as the heating power increases, while the electron density at the top of the pedestal remains nearly unchanged. Unfortunately, the value of pedestal width is not available in the database. If one assumes that the pedestal width remains constant as heating power increases, the increasing values of the pedestal parameters, such as pedestal pressure and temperature, are likely to be the result of the improvement in the edge stability. In several experiments, it was found that the pedestal width is independent of the heating power. For example, in Ref. [16], in the Alcator C-MOD experiment where the edge proles were obtained using high resolution edge Thomson scattering, it was observed that the pedestal width is independent of the heating power.

4. SIMULATION RESULTS AND DISCUSSION

The simulations are carried out during the quasi-stationary period of the H-mode phase of each discharge (see Fig.1). The anomalous transport in the core is calculated using the Mixed Bohm/ gyro-Bohm transport model [7]. The transport within the pedestal between ELM crashes is assumed to be the ion neoclassical transport at top of the pedestal computed using NCLASS [17]. Since the experimentally measured edge proles for these discharges do not have enough resolution to resolve the width of the barrier, the pedestal width is either set equal to 3 cm or is calculated assuming that the width scales with the ion Larmor radius. Other pedestal width scalings that have been proposed include the pedestal width based on magnetic and ow shear stabilization [18], the pedestal width based on normalized poloidal pressure [19], or the pedestal width based on ion orbit loss [20]. However, the results presented in this paper regarding the power dependence of the pedestal, do not appear to be sensitive to the scaling used for the pedestal width.

4.1 JETTO SIMULATIONS WITH ELMS TRIGGERED BY PRESSURE-DRIVEN BALLOONING MODES

In this section, simulations are described for the JET power scan discharges, which are carried out using the JETTO code with the assumption that each ELM crash is triggered by a pressure-driven ballooning mode. If anywhere within the pedestal, the normalized pressure gradient, , exceeds the critical value of the normalized pressure gradient, α_c, that is

$$\alpha \equiv - \frac{2\mu_0 q^2}{\epsilon B_T^2} \frac{\partial p}{\partial \rho} > \alpha_c, \qquad (2)$$

an ELM crash occurs in the simulation. The numerical value of c is chosen and, then, adjusted to be consistent with the HELENA and MISHKA stability code results. The details of the treatment during thecrash is described in the Section IIA.

In Fig. 2, the electron pressure proles obtained from simulations of discharges 44018, 44029 and 44013 are plotted at the time just before an ELM crash. Note that discharges 44018, 44029 and 44013 have an NBI heating power of 8.1MW, 11.3 MW and 13.9MW, respectively. It can be seen from thegure that the core pressure proles are higher in the simulation for the discharges with higher heating power, but the pressure at the top of the pedestal is almost same for the three discharges. This result for the pressure at the top of the pedestal is inconsistent with the experimental observation in which the pressure at the top of the pedestal increases with heating power.

The pressure at the top of the pedestal can be approximated by the product of the pedestal width and the pedestal gradient. Consequently, the disagreement between the simulations in Fig. 2 and experimental data could result from the width model. (A fixed value of 3 cm for the pedestal width is used in the simulations shown in Fig.2.) Therefore, simulations are carried out using a dierent width scaling in order to test the sensitivity of the simulations to the pedestal width model. Specically, simulations are carried out for the JET discharges using a pedestal width that scales as the ion Larmor radius. As can be seen in Fig.3, it is found that the electron pressure at the top of the pedestal is again nearly independent of heating power. Thus, the model in which the pedestal width is a function of the ion Larmor radius combined with ELMs triggered by pressure-driven ballooning modes does not yield simulations that agree with the experimental result of increased pedestal pressure with increased heating power.

4.2 JETTO SIMULATIONS WITH ELMS TRIGGERED BY CURRENT-DRIVEN PEELING MODES

In this section, JETTO simulations for discharges in the JET power scan are carried out with the assumption that each ELM crash can be triggered by current-driven peeling modes. For the ELMs triggered by a current-driven peeling mode, the criteria used is that the current density in the pedestal exceeds a critical current density. This critical current density model is based on an analytical expression developed in Ref. [11]. For axisymmetric toroidal geometry, thecurrent-driven peeling instability condition is

$$\sqrt{1 - 4D_M} < 1 + \frac{2}{2\pi q'} \oint \frac{j_{||} B_T \, dl}{R^2 B_p^3} \, dl \tag{3}$$

where D_M is the Mercier coefficient; q' is the derivative of the safety factor with respect to the poloidal flux surface coordinate; $j_{||}$ is the current density parallel to the magneticeld B ; R is the major radius; B_p is the poloidal magneticeld; and *dl* is the poloidal arc length element on a flux surface.

Figure 4 shows the electron pressure proles obtained from simulations at a time just before an ELM crash for the three discharges 44018 (8.1MW), 44029 (11.3MW) and 44013 (13.9MW). Note

that the horizontal scale in Fig.4 represents only the outer 10% of the plasma. These simulations are carried out with axed pedestal width of 3cm. It can be seen that the values of electron pressure at the top of the pedestal for discharge 44018, 44029 and 44013 are 6.10, 6.52 and 7.33kPa, respectively so that the electron pressure at the top of the pedestal increases as the heating power increases. These results indicate a trend that is similar to the experimental data presented in Table III. From the experimental data, the relation between the electron pressure at the top of the pedestal and the heating power is approximately

$$p_{\mathrm{e,ped,exp}} \propto P_{\mathrm{heating}}^{0.5}. \tag{4}$$

For the simulations using ELMs triggered by current-driven peeling modes, shown in Fig.4, it is found that the electron pressure at the top of the pedestal scales with the heating power as

$$p_{\mathrm{e,ped,sim}} \propto P_{\mathrm{heating}}^{0.3}. \tag{5}$$

Thus, the simulations with ELMs triggered by current-driven peeling modes yield a some-what weaker dependence of the electron pressure at the top of the pedestal as a function of heating power than that indicated by experimental data.

Figure 5 shows the simulated plasma current density and bootstrap current density profiles at a time just before an ELM crash for all three discharges. It can be seen in the top panel in Fig.5 that the current density rises to a peak in the steep gradient region of the pedestal at the edge of the plasma and the peak values of the current density in the pedestal region are almost the same for the three discharges. The main contribution to the edge current density is the bootstrap current density shown in the bottom panel in Fig.5. The bootstrap current density is large near the edge of the plasma mainly because of the strong pressure gradient which generates bootstrap current within the pedestal. Note that, according to neoclassical theory, the bootstrap current density is approximately proportional to the pressure gradient and inversely proportional to the square root of the collisionality.

In Fig.6, the total current and bootstrap current densities are plotted for the time interval between two consecutive ELM crashes at the normalized minor radius of 0.97 (r/a = 0.97) for the low power discharge 44018 and the high power discharge 44013. Note, the normalized minor radius of 0.97 is in the region within the pedestal, but close to the top of the pedestal.

It can be seen that the total and bootstrap current densities rise more quickly after an ELM crash in the higher power discharge than do the corresponding current densities in the low power discharge. At the time, just before an ELM crash (at the current peak), it can be seen that the bootstrap current density is less than the total current density in the low power discharge (44018) while the bootstrap current density is larger than total current density in the high power discharge (44013). This result can be explained as follows: In the high power discharge (44013), the bootstrap current density increases very quickly due to a rapid rise of pressure gradient, but the rise in the total current

density is slowed down by a back electro-motive force. As a result, the bootstrap current density is larger than the total current density just before an ELM crash in the higher power discharge. In the low power discharge (44018), the bootstrap current increases more slowly, resulting in a smaller back electro-motive force and, as a consequence, the total current density is larger than the bootstrap current density in that case. The simulations indicate that, although the critical current density that results in the current-driven instability does not depend on the injected power, the bootstrap current density and the related pressure gradient in the pedestal do increase with increasing power.

4.3 STABILITY ANALYSIS

Stability analyses are performed to evaluate the edge stability at the time just before an ELM crash for simulations in Fig.4 using the HELENA and MISHKA stability codes. Note that simulations in Fig. 4 are carried with the assumption that each ELM crash can be triggered by current-driven peeling modes. The version of the MISHKA code used in these analyses considers only the ideal MHD modes. On the stability s-α diagrams, the unstable infinite-*n* ideal ballooning, finite-*n* ballooning and low-*n* kink (peeling) modes are indicated.

The toroidal mode numbers, n, included in the MISHKA code analysis range from 1 to 14. Figs. 7, 8 and 9 show the stability s-α diagrams for discharges 44018, 44029 and 44013, respectively. Note that the toroidal mode number n shown on the stability s-α diagram are the most unstable modes. Only unstable modes with the growth rates greater than 0.03 of the Alfven frequency are included in Figs.7, 8 and 9. A weakly unstable mode might be stabilized if a stabilizing eect such as thenite Larmor radius or the ion diamagnetic drift effect were included. A discussion of this stabilizing eect is beyond the scope of this study.

It can be seen that at the 95% flux surface (near the top of the H-mode pedestal), the plasma is unstable as a consequence of the n = 3 toroidal mode in each case. Note that the magnetic shear near the edge of plasma is relatively low for the discharges considered in the power scan. It can also be seen in Figs. 7, 8 and 9 that the shape of the unstable regions in the stability s- diagram are similar, but that the normalized pressure gradient, , associated with the 95% ux surface increases as the heating power increases. For discharges 44018 (8.1MW), 44029 (11.3MW) and 44013 (13.9MW), the maximum values of the normalized pressure gradient, α, are 4.4, 4.9 and 5.2, respectively.

CONCLUSION

Simulations of H-mode discharges in a JET power scan are carried out using the JETTO code. Predictive pedestal and core models are used together in these simulations. It is found that the ELMs triggered by the current-driven peeling modes in these simulations can explain the increase in pedestal pressure as the heating power increases. In the stability analyses carried out, it is found that for these discharges the edge pressure gradient and the edge current is limited by low-n kink (peeling) modes.

ACKNOWLEDGEMENTS

One author (T. Onjun) thanks the Royal Thai Government and the Development and Promotion for Science and Technology Talents Project of Thailand (DPST) for their support. This work was conducted partly under European Fusion Development Agreement. It was supported in part by the U.S. Department of Energy (DOE) under contract No. DE-FG02- 92-ER-5414 and by the UK Department of Trade and Industry and by EURATOM.

REFERENCES

[1]. G. Saibene et al., Nucl. Fusion **39**, 1133 (1999).

[2]. J. Kinsey, T. Onjun, G. Bateman, et al. , in Preceeding of the IAEA Conference (TH/P1-09) (2002).

[3]. T. Onjun, G. Bateman, A. H. Kritz, and G. Hammett, Phys. Plasmas **9**, 5018 (2002).

[4]. J. G. Cordey et al., in Preceeding of the IAEA Conference (IAEA-CN-94/CT/P-02) (2002).

[5]. G. Cenacchi and A. Taroni, JET-IR(88) **03** (1988).

[6]. A. B. Mikhailovskii, G. T. A. Huysmans, S. E. Sharapov, and W. Kerner, Plasma Phys. Rep **23**, 844 (1997).

[7]. M. Erba, A. Cherubini, V. V. Parail, et al., Plasma Physics and Controlled Fusion **39**, 261 (1997).

[8]. H. R. Wilson, J. W. Connor, A. R. Field, et al., Phys. Plasmas 6 , 1925 (1999).

[9]. P. Gohil, Phys. Rev. Letters 61 , 1603 (1988).

[10]. G. T. A. Huysmans et al., in Proceeding of the 22nd EPS Conference on Controlled Fusion and Plasma Phys. Part I (1995).

[11]. J. W. Connor, H. R. Hastie, H. R. Wilson, and R. L. Miller, Phys. Plasmas **5**, 2687 (1998).

[12]. H. R. Wilson and R. L. Miller, Phys. Plasmas **6**, 873 (1999).

[13]. J. Manickam, Phys. Fluids B4 (1992).

[14]. R. Aymar, P. Barabaschi, and Y. S. (for the ITER Team), Plasma Phys. Control. Fusion **44**, 519 (2002).

[15]. T. Hatae, M. Sugihara, A. E. Hubbard, et al., Nucl. Fusion **41**, 285 (2001).

[16]. J. W. Hughes, D. A. Mosseessian, A. E. Hubbard, B. LaBombard, and E. S. Marmar, Phys. Plasmas **9**, 3019 (2002).

[17]. W. A. Houlberg, K. C. Shaing, S. P. Hirshman, and M. C. Zarnstor, Phys. Plasmas **4**, 3231 (1997).

[18]. M. Sugihara, Y. Igitkhanov, G. Janeschitz, et al., Nucl. Fusion **40**, 1743 (2000).

[19]. T. Osborne, K. H. Burrell, R. J. Groebner, et al. , Nucl.Mater. **266-269**, 131 (1999).

[20]. K. C. Shang, Phys. Fluids **B4**, 290 (1992).

Plasma Parameters	Pulse No: 44018	Pulse No: 44029	Pulse No: 44013
R(m)	2.90	2.90	2.91
a(m)	0.94	0.94	0.94
B_T (T)	2.77	2.77	2.76
I_P (MA)	2.57	2.57	2.57
κ	1.75	1.75	1.75
δ	0.22	0.23	0.23
A_H (AMU)	1.97	2.00	1.99
Z_{eff}	1.91	2.05	2.14
n_l (10^{19} particles/m^3)	5.60	5.82	5.82
P_{NBI} (MW)	8.1	11.3	13.9

TABLE I: Plasma parameters for the discharges used in the Power Scan. The plasma parameters (and associated units) are described in Table II.

Symbol	Units	Description
a	*m*	Plasma Minor Radius (Half-width)
r	*m*	Flux Surface Minor Radius (Half-width)
R	*m*	Major Radius to Geometric Center of Each Flux Surface
ρ		Toroidal Flux Co-ordinate
κ		Plasma Elongation
δ		Plasma Triangularity
B_T	*Tesla*	Vacuum Toroidal Magnetic Field at R
I_P	*MA*	Plasma Current
A_H	*AMU*	Hydrogenic Isotope Mass
Z_{eff}		Effective Charge
n_l	10^{19} *particles/*m^3	Line Average Density
W_{ped}	*MJ*	Stored Energy in Pedestal Region
$T_{e,\,ped}$	*keV*	Electron Temperature at the Top of the Pedestal
$n_{e,\,ped}$	10^{19} *particles/*m^3	Electron Density at the Top of the Pedestal
$\bar{n}_{20}$	10^{20} *particles/*m^3	Line Average Electron Density
$p_{e,\,ped}$	*kPa*	Electron Pressure at the Top of the Pedestal
P_{NBI}	*MW*	NBI Heating Power

TABLE II: Notation used in this paper.

	Pulse No: 44018	Pulse No: 44029	Pulse No: 44013
$T_{e,ped}$	0.72	0.85	0.97
$n_{e,ped}$	4.75	4.76	4.61
$p_{e,ped}$	5.47	6.43	7.16

TABLE III: Pedestal parameters before ELMs obtained from the ITPA Pedestal Database

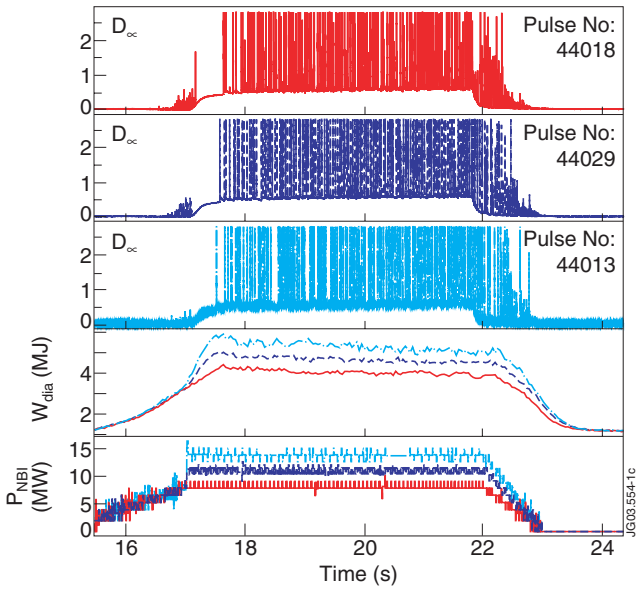

Figure1: The time history of the Dα signal measured at the edge of the plasma, the stored energy and the heating power are shown for JET discharges 44018 (8.1MW), 44029 (11.3MW) and 44013 (13.9MW). The bottom two panels illustrate the stored energy increases with increasing heating.

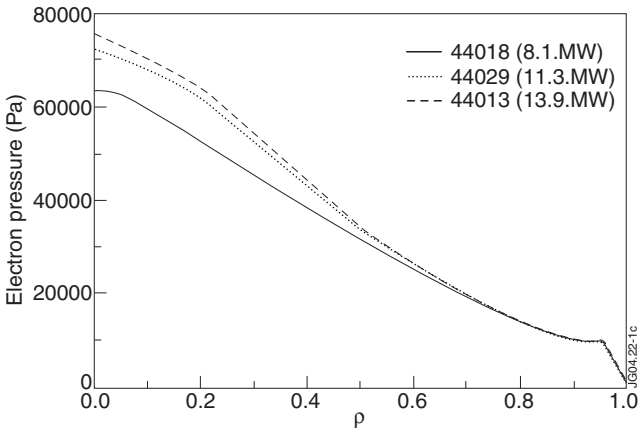

Figure 2: The predicted pressure profiles are plotted at the time just before ELMs for JET discharges 44018 (8.1MW), 44029 (11.3MW) and 44013 (13.9MW). These simulations are carried out using JETTO code with ELMs triggered by ballooning mode and a fixed pedestal width of 3cm.

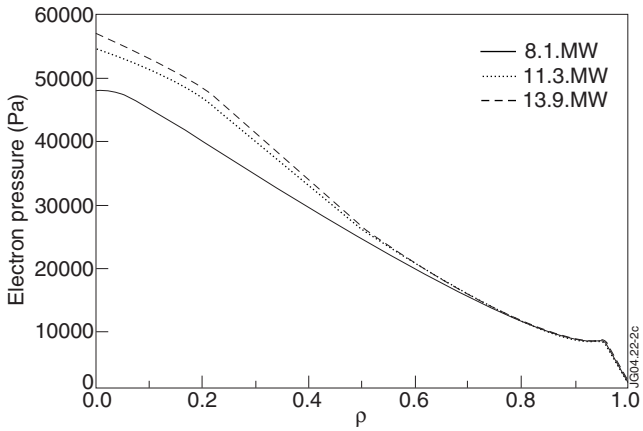

Figure 3: The predicted pressure profiles are plotted at the time just before ELMs for JET discharges 44018 (8.1MW), 44029 (11.3MW) and 44013 (13.9MW). These simulations are carried out using JETTO code with ELMs triggered by pressure-driven ballooning mode alone and a pedestal width scales with the Larmor radius.

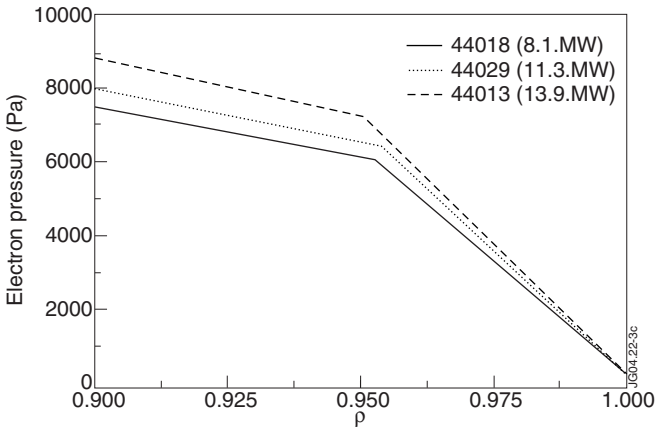

Figure 4: The predicted pressure profiles are plotted at the time just before ELMs for JET discharges 44018 (8.1MW), 44029 (11.3MW) and 44013 (13.9MW). These simulations are carried out using the JETTO code with ELMs triggered by current-driven peeling modes and a fixed pedestal width of 3cm.

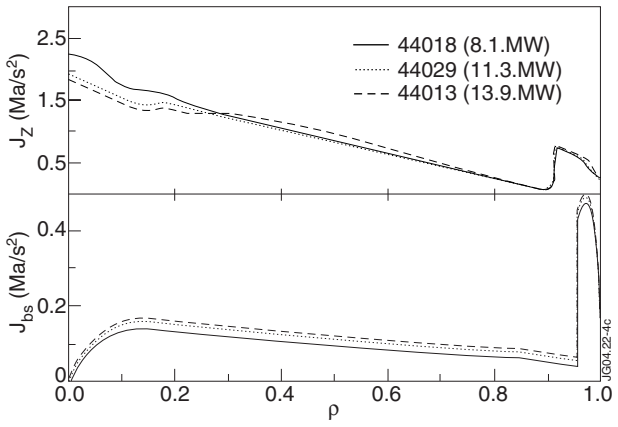

Figure 5: The plasma current (top panel) and bootstrap current (bottom panel) profiles is plotted at the time just before ELMs for all three discharges.

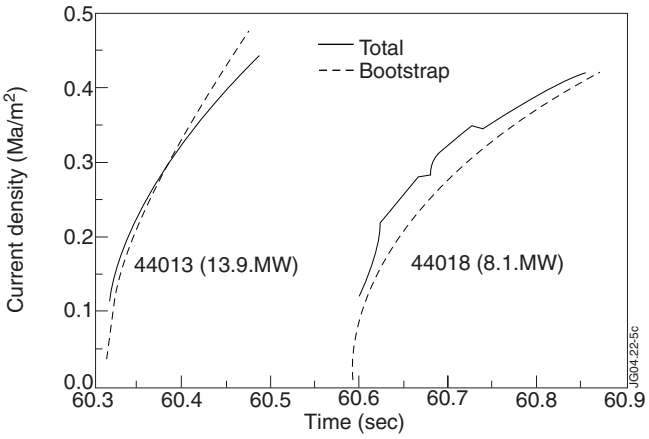

Figure 6: The plasma current and bootstrap current at a normalized minor radius of 0.97 is plotted as a function of time for the low power (44018) and high power (44013) discharges. These results are obtained from the simulations with ELMs triggered by current-driven peeling modes.

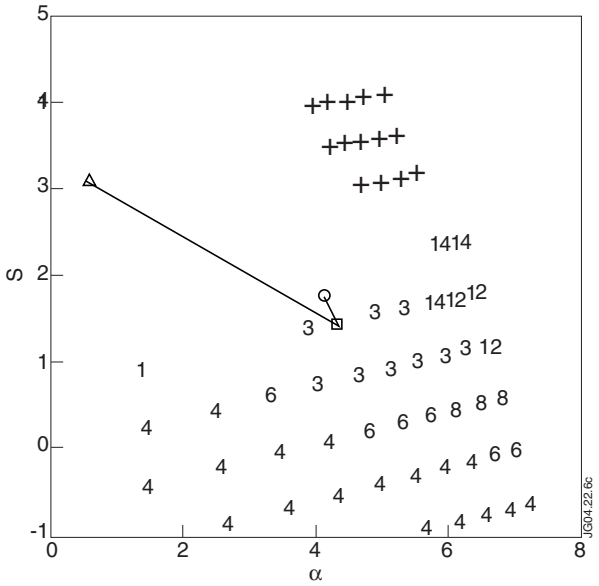

Figure 7: Stability results obtained using the HELENA and MISHKA stability codes are plotted on an s-α stability diagram for JET discharge 44018 (8.1MW). The region of instability associated with the infinite-n ideal ballooning modes is indicated with crosses. The numbers indicate the most unstablenite-n ballooning and low-n kink (peeling) modes at each location on the s-α plane. Higher mode numbers (n≥10) correspond to finite-n ballooning modes. The region without numbers or crosses is the region where all modes are stable. The values of s and α at the 92%, 95% (top of the pedestal) and 97% flux surface are indicated by △, □, and ○, respectively.

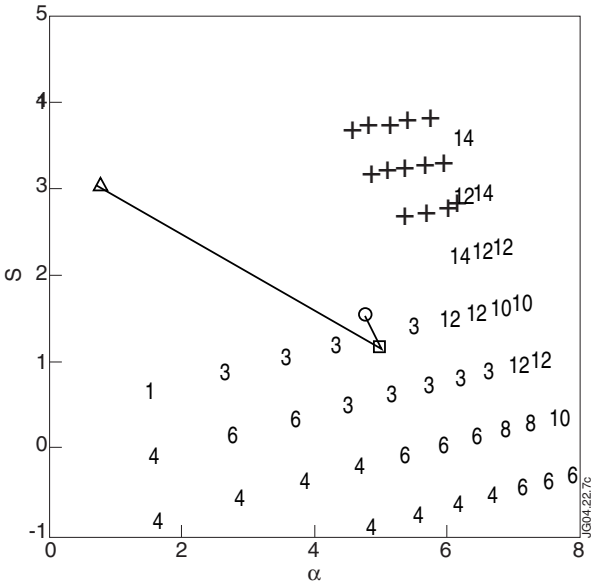

Figure 8: Stability results obtained using the HELENA and MISHKA stability codes are plotted on an s-α stability diagram for JET discharge 44029 (11.3MW). The region of instability associated with the infinite-n ideal ballooning modes is indicated with crosses. The numbers indicate the most unstable finite-n ballooning and low-n kink (peeling) modes at each location on the s-α plane. Higher mode numbers (n≥10) correspond to finite-n ballooning modes. The region without numbers or crosses is the region where all modes are stable. The values of s and at the 92%, 95% (top of the pedestal) and 97% flux surface are indicated by △, □, and ○, respectively.

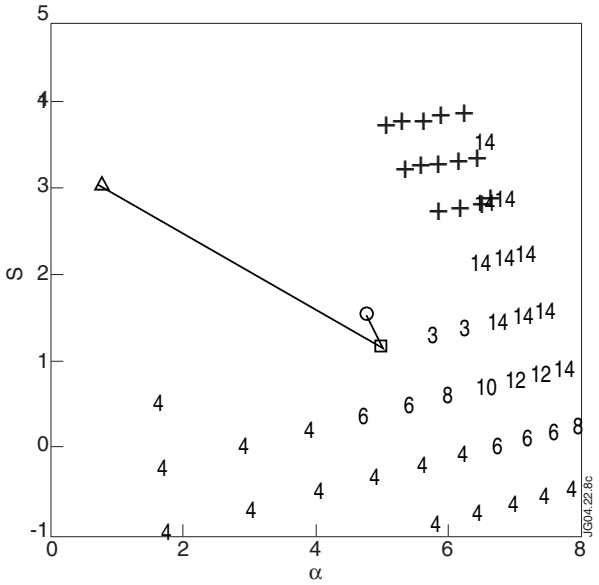

Figure 9: Stability results obtained using the HELENA and MISHKA stability codes are plotted on an s-α stability diagram for JET discharge 44013 (13.9MW). The region of instability associated with the infinite-n ideal ballooning modes is indicated with crosses. The numbers indicate the most unstable finite-n ballooning and low-n kink (peeling) modes at each location on the s-α plane. Higher mode numbers (n≥10) correspond to finite-n ballooning modes. The region without numbers or crosses is the region where all modes are stable. The values of s and α at the 92%, 95% (top of the pedestal) and 97% flux surface are indicated by △,□, and○, respectively